[O I] 63 μm JETS IN CLASS 0 SOURCES DETECTED BY *HERSCHEL*

B. Nisini[1], G. Santangelo[1,2], T. Giannini[1], S. Antoniucci[1], S. Cabrit[3], C. Codella[2], C. J. Davis[4], J. Eislöffel[5],
L. Kristensen[6], G. Herczeg[7], D. Neufeld[8], AND E. F. VAN Dishoeck[9,10]

[1] INAF—Osservatorio Astronomico di Roma, via Frascati 33, I-00040 Monte Porzio, Italy
[2] INAF—Osservatorio Astrofisico di Arcetri, Largo E. Fermi 5, I-50125 Firenze, Italy
[3] LERMA, Observatoire de Paris, UMR 8112 of the CNRS, 61 Av. de L'Observatoire, F-75014 Paris, France
[4] Astrophysics Research Institute, Liverpool John Moores University, Liverpool, UK
[5] Thüringer Landessternwarte, Sternwarte 5, D-07778, Tautenburg, Germany
[6] Harvard-Smithsonian Center for Astrophysics, 60 Garden Street, Cambridge, MA 02138, USA
[7] Kavli Institute for Astronomy and Astrophysics, Peking University, Yi He Yuan Lu 5, Haidian Qu, Beijing 100871, China
[8] Department of Physics and Astronomy, Johns Hopkins University, 3400 North Charles Street, Baltimore, MD 21218, USA
[9] Sterrewacht Leiden, Leiden University, PO Box 9513, 2300 RA, Leiden, The Netherlands
[10] Max-Planck-Institut fr extraterrestriche Physik, Postfach 1312, D-85741, Garching, Germany

ABSTRACT

We present *Herschel* PACS mapping observations of the [O I] 63 μm line toward protostellar outflows in the L1448, NGC 1333-*IRAS*4, HH 46, BHR 71, and VLA 1623 star-forming regions. We detect emission spatially resolved along the outflow direction, which can be associated with a low-excitation atomic jet. In the L1448-C, HH 46 IRS, and BHR 71 IRS1 outflows this emission is kinematically resolved into blue- and redshifted jet lobes, having radial velocities up to 200 km s^{-1}. In the L1448-C atomic jet the velocity increases with the distance from the protostar, similarly to what is observed in the SiO jet associated with this source. This suggests that [O I] and molecular gas are kinematically connected and that the latter could represent the colder cocoon of a jet at higher excitation. Mass flux rates ($\dot{M}_{jet}(O I)$) have been measured from the [O I] 63 μm luminosity adopting two independent methods. We find values in the range $(1–4) \times 10^{-7} M_\odot$ yr^{-1} for all sources except HH 46, for which an order of magnitude higher value is estimated. $\dot{M}_{jet}(O I)$ are compared with mass accretion rates ($\dot{M}_{acc}$) onto the protostar and with $\dot{M}_{jet}$ derived from ground-based CO observations. $\dot{M}_{jet}(O I)/\dot{M}_{acc}$ ratios are in the range 0.05–0.5, similar to the values for more evolved sources. $\dot{M}_{jet}(O I)$ in HH 46 IRS and *IRAS*4A are comparable to $\dot{M}_{jet}(CO)$, while those of the remaining sources are significantly lower than the corresponding $\dot{M}_{jet}(CO)$. We speculate that for these three sources most of the mass flux is carried out by a molecular jet, while the warm atomic gas does not significantly contribute to the dynamics of the system.

Key words: ISM: clouds – ISM: jets and outflows – stars: formation

1. INTRODUCTION

Collimated and high-velocity mass ejections are often associated with young stellar objects (YSOs), being a natural outcome of the protostellar accretion process. Indeed, collimated jets have been observed in a variety of YSOs of different evolutionary stages, from the embedded Class 0 protostars to pre-main-sequence classical T Tauri stars (CTTSs), although the excitation conditions, and consequently the suitable observational tracers, vary significantly for the different sources (e.g., Frank et al. 2014). Jets from CTTSs have been investigated in the most detail, since they are optically visible and can be studied through several emission lines tracing hot gas ($\gtrsim 10^4$ K; e.g., Hartigan & Morse 2007; Podio et al. 2012). More embedded Class I sources are mainly observed in the near-IR. Compared to CTTS jets, Class I jets are denser, colder, and less ionized, showing also a significant molecular component (e.g., Garcia Lopez et al. 2008; Davis et al. 2011).

In the less evolved and heavily obscured Class 0 objects, jets are only sporadically detected in the submillimeter as collimated high-velocity emission of CO and SiO gas at relatively low excitation (~100–300 K; e.g., Gueth & Guilloteau 1999; Tafalla et al. 2004; Codella et al. 2007; Hirano et al. 2010). Most of the Class 0 sources, however, are associated with large-scale, low-velocity molecular CO emission, tracing cavities or swept-up gas, without any clear evidence of the

underlying jet or wind pushing away the ambient gas. The above scenario poses the following questions: What is the agent driving the large-scale molecular outflows in Class 0 sources? Is the low-excitation collimated molecular jet seen in some Class 0 sources dynamically important in the mass accretion/ejection balance? Why do only a few Class 0 sources have collimated molecular jets?

Indeed, the study of jets in Class 0 sources suffers from a strong observational bias. Since these sources are still deeply embedded in their parental cloud, any optical/near-IR emission near the source escapes from detection. In addition, given the expected dense environment, it is likely that a significant part of the jet material is composed of neutral atomic gas at relatively low temperatures (e.g., ~1000–4000 K) whose emission lines fall in the mid- and far-IR spectral range. Gas with such properties has been revealed by recent *Spitzer* observations of young stars, showing the presence of low-excitation forbidden lines of [Si II], [S I], and [Fe II] close to the central protostar (Dionatos et al. 2009; Neufeld et al. 2009; Lahuis et al. 2010; Baldovin-Saavedra et al. 2011).

Determining the dynamical properties of this atomic jet is extremely important in order to understand the feedback of the active accretion on the surrounding medium and the formation of large-scale CO outflows. In addition, the mass flux rate carried out by such a jet can give information on the ejection/

accretion efficiency and, when compared to sources with different ages, its evolution.

Among the tracers of low-excitation atomic jets, the [O I] 63 μm line is expected to be the brightest, owing to the high abundance of atomic oxygen and favorable excitation conditions. In particular, for preshock densities $<10^5$ cm^{-3} the [O I] 63 μm line is predicted to be the main coolant in the original wind shock, i.e., the dissociative shock caused by the impact of the high-velocity collimated wind ejected from the protostar on the surrounding material (Hollenbach & McKee 1989). As such, its luminosity is directly proportional to the wind mass flux rate for a wide range of shock conditions (Hollenbach 1985).

Strong [O I] emission has been observed in the past toward young protostars and their associated outflows, with the first detections obtained by the Kuiper Airborne Observatory (Ceccarelli et al. 1997) and subsequent systematic surveys performed with the *Infrared Space Observatory* (*ISO*; Giannini et al. 2001; Nisini et al. 2002; Liseau et al. 2006). In these studies, the importance of [O I] 63 μm line emission on the protostellar gas cooling has been addressed, together with its role as a tracer of the original wind driving molecular outflows (Giannini et al. 2001). However, the coarse spatial and spectral resolution of these *ISO* observations (80″ and $R \sim 300$) yields limited morphological and kinematical information on the [O I] emission, which does not allow us to unequivocally associate it with the protostellar jet. The Photodetector Array Camera and Spectrometer (PACS; Poglitsch et al. 2010) instrument on board the *Herschel Space Observatory* (Pilbratt et al. 2010) provides a factor of 10 improvement in spatial resolution with respect to *ISO* and spectral resolution $R \sim 3500$, allowing one to detect weak lines on a strong continuum and resolve gas at velocities $\gtrsim 100$ km s^{-1} (e.g., Van Kempen et al. 2010; Karska et al. 2013). In addition, the mapping capability of PACS, although limited, is well suited to cover in few observational settings not only the protostellar environment but also most of the outflow region.

PACS observations of the [O I] 63 μm line have been performed on samples of YSOs of both Class 0/I (Green et al. 2013; Karska et al. 2013) and CTTS (Podio et al. 2012) type, as well as toward individual shock regions along outflows (Benedettini et al. 2012; Santangelo et al. 2013). These observations were obtained with a single footprint measurement on the targeted objects, thus providing only limited spatial information. In these studies, the [O I] 63 μm emission was compared with other tracers of gas cooling, namely, H$_2$O, CO, and OH, as well as with available shock and photodissociation region (PDR) models. The results of this comparison all concur to indicate that [O I] emission both close to the source and on specific shock positions comes from high-velocity dissociative shocks, and not from the shock responsible for the molecular emission, confirming previous findings obtained with *ISO*.

Here we present extensive PACS mapping of the [O I] lines at 63 and 145 μm in a sample of outflows from young low-mass protostars, located in the L1448, NGC 1333-*IRAS*4, BHR 71, VLA 1623, and HH 46 star-forming regions. The sources have been chosen among outflows observed by *ISO* and/or *Spitzer* for being associated with warm gas emission and having extended outflows.

In particular, this paper is focused on the identification of the atomic jet emission associated with the large-scale molecular outflows and inferring its role in the dynamics of the system. In

Table 1
Observed Outflows

Source	R.A. (J2000)[a]	Decl. (J2000)[a]	D	L_{bol}[b]
	(h m s)	(° ′ ″)	(pc)	($L_\odot$)
L1448	03 25 38.79	+30 44 09.32	232	9
NGC 1333-*IRAS*4	03 29 10.58	+31 13 24.37	235	9.1
HH 46	08 25 43.90	−51 00 36.0	450	27.9
BHR 71	12 01 35.44	−65 08 55.97	200	14.8
VLA 1623	16 26 26.46	−24 24 24.78	120	1.1

[a] Coordinates of the central map position.
[b] From Kristensen et al. (2012) except for VLA 1623, where L_{bol}^b is taken from Murillo et al. (2013).

Section 2 we describe the observations performed, discuss our data reduction procedure, and present the [O I] 63 μm line maps. The morphology of the observed emission is described in Section 3, where we also discuss the kinematics of the [O I] 63 μm gas in the sources where the line has been resolved in velocity (namely, L1448-C, HH 46 IRS, and BHR 71 IRS1). In Section 4 we present the methods adopted to derive the mass flux rate carried out by the atomic gas traced by the [O I] 63 μm emission, discussing the associated uncertainty and assumptions. Finally, in Section 5 we discuss how the measured [O I] 63 μm mass flux rate can be related to the molecular outflow thrust and to the protostellar mass accretion rate.

2. OBSERVATIONS

Observations with the PACS instrument in the L1448, NGC 1333-*IRAS*4, BHR 71, and VLA 1623 regions were performed as part of the OT1 program "Probing the physics and dynamics of the hidden warm gas in the youngest protostellar outflows" (OT1_bnisini_1). In addition, a map of the [O I] 63 μm emission along the HH 46 IRS outflow, obtained as part of the "Water In Star formation with Herschel" key program (van Dishoeck et al. 2011), is also presented here. Table 1 provides the central coordinates of the maps, together with distance of the region and luminosity of the outflow-driving source considered in the analysis.

PACS integral field unit (IFU) line spectroscopy was used in chopping/nodding mode to obtain spectral maps of the outflows at the [O I] transition $^3P_1 - ^3P_2$ (63.1852 μm observed in the second grating order). For the four outflows of the OT1_bnisini_1 program, simultaneous observations of the $^3P_0 - ^3P_1$ (145.5254 μm) transition (in the first PACS grating order) were also taken.

The IFU consists of a 5 × 5 spatial pixel (called spaxels) array providing a spatial sampling of 9″4 spaxel^{-1}, for a total field of view of 47″ × 47″. The diffraction-limited FWHM beam size at 63 μm (145 μm) is ~5″ (11″).

The outflows were covered through Nyquist-sampled raster maps arranged along the outflow axis. The extent of the mapped regions is delineated in Figures 1–5 as green polygons. The nominal spectral resolutions of the grating at 63 μm and 145 μm are $R \sim 3500$ and 1200, respectively, which correspond to the velocity resolutions of ~86 and 250 km s^{-1}, respectively. In-flight calibrations, however, have shown that the PACS effective spectral resolution at 63 μm could span from 100 to 130 km s^{-1} (according to the PACS observer manual[11]). To

---

[11] http://herschel.esac.esa.int/Docs/PACS/html/pacs_om.html

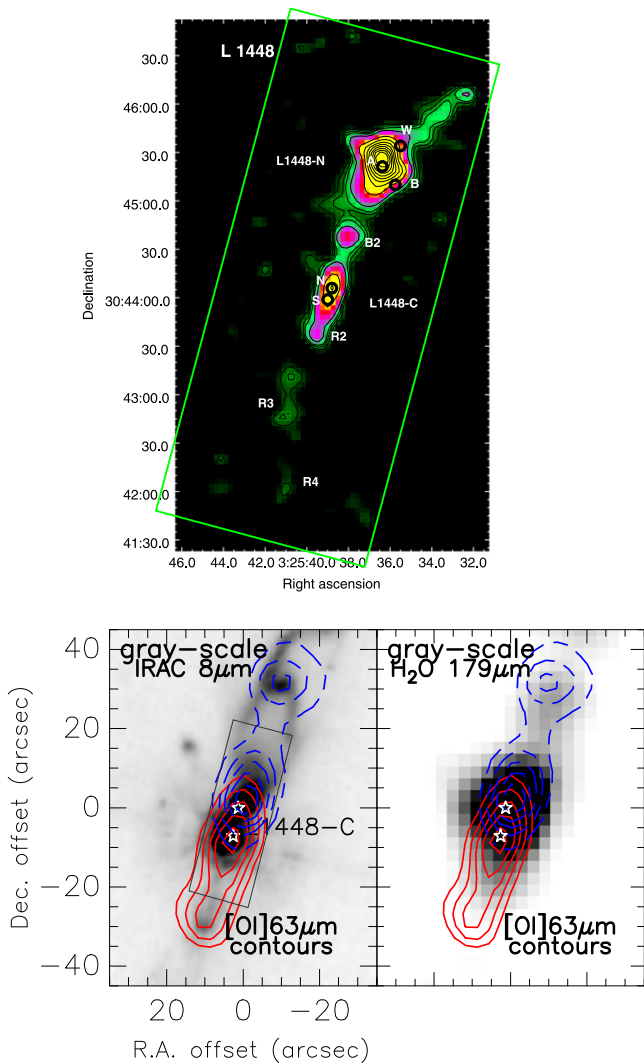**Figure 1.** Upper panel: continuum-subtracted PACS map of the [O I] 63 μm toward L1448. Labels indicate the positions of the protostars in the region, namely, L1448 C-N and C-S, at the center, and L1448 N-A, N-B, and N-W, in the northern region, as well as the main emission peaks following the nomenclature for CO of Bachiller et al. (1990). The green rectangle delimits the region mapped with PACS. Lower panel: enlargement of the L1448-C central region, where blue- and redshifted [O I] 63 μm emission is displayed with dashed and solid contours, respectively. V_{LSR} integration limits are −200 to 0 km s^{-1} and 0 to +200 km s^{-1} for the blue- and redshifted emission, respectively. Contours are drawn from 2 × 10^{-5} to 6 × 10^{-5} erg s^{-1} cm^{-2} sr^{-1} in steps of 1 × 10^{-5} erg s^{-1} cm^{-2} sr^{-1}. The contours are overlayed on a grayscale *Spitzer*-IRAC archival image (left) and on a PACS map of the H$_2$O 179 μm line (from Nisini et al. 2013). The gray box delineates the region where the jet integrated flux has been extracted.

Figure 2. Same as in Figure 1, but for *IRAS*4A and B (with the 4.5 μm *Spitzer* image in place of the 8 μm image). Contours refer to the total integrated line intensity and run from 1.5 × 10^{-5} to 7.5 × 10^{-5} erg s^{-1} cm^{-2} sr^{-1} in steps of 1.5 × 10^{-5} erg s^{-1} cm^{-2} sr^{-1}.

evaluate the instrumental FWHM in our observations, we have extracted an [O I] 63 μm spectrum toward the PDR region located northeast of VLA 1623 (see Appendix A), under the assumption that the intrinsic line width is negligible (i.e., below 10 km s^{-1}). The line width of the unresolved line is on the order of 130 km s^{-1}, which we hereafter consider our instrumental limit.

The data of the L1448, NGC 1333-*IRAS*4, BHR 71, and VLA 1623 sources were acquired with a sampling of 44 km s^{-1} per spectral element (i.e., Nyquist sampling at the nominal resolution). A factor of two higher spectral sampling was instead adopted for the observations of HH 46 (22 km s^{-1} per spectral element). The observations were performed with a

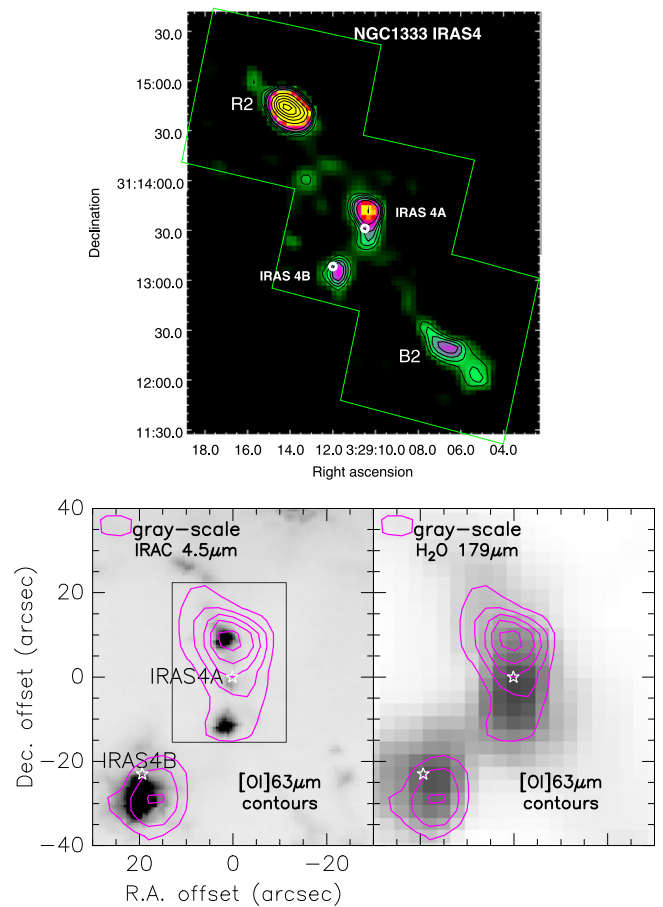single scan cycle, providing an integration time per spectral resolution element of 30 s.

All the data were reduced with HIPE[12] v10.0, where they were flat-fielded and flux-calibrated by comparison with observations of Neptune. The flux calibration uncertainty amounts to around 20%, while the *Herschel* pointing accuracy is ~2″. Finally, in-house IDL routines were used to locally fit and remove the continuum emission and to construct integrated line maps.

3. [O I] MORPHOLOGY AND KINEMATICS

Figures 1–5 show the [O I] 63 μm maps of the five observed outflows. The morphology of the [O I] 145 μm line emission is very similar to that of the 63 μm line, but images have a lower signal-to-noise ratio and will not be presented here. The 145 μm data will be used to estimate the gas density, as described in Section 4.1.1. The main outflow properties and the general distribution of the [O I] 63 μm emission are discussed in Appendix A. The obtained maps cover several protostars, most of them associated with their own outflow. Here we discuss in more detail only the properties of the most prominent outflows in each region and discuss the morphology and
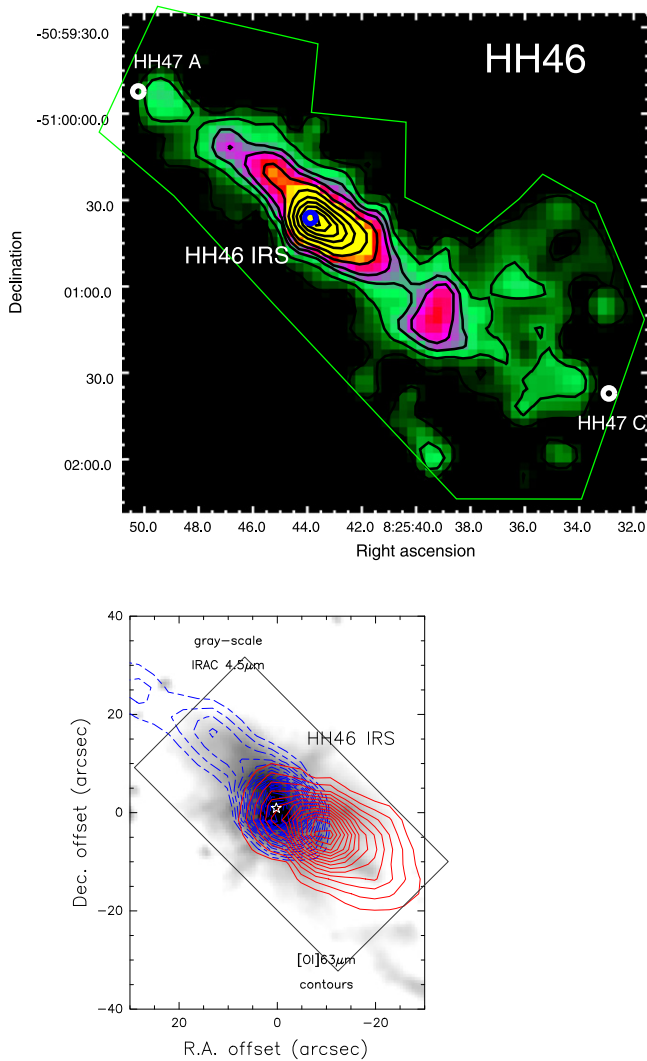

Figure 3. As in Figure 1, but for HH 46. In this case, however, the H_2O image is not available. Blue- and redshifted contours run from 2×10^{-5} to 2×10^{-4} erg s^{-1} cm^{-2} sr^{-1} in steps of 1×10^{-5} erg s^{-1} cm^{-2} sr^{-1}. Velocity integration limits are -400 to 0 km s^{-1} and 0 to $+400$ km s^{-1} for the blue- and redshifted emission, respectively.
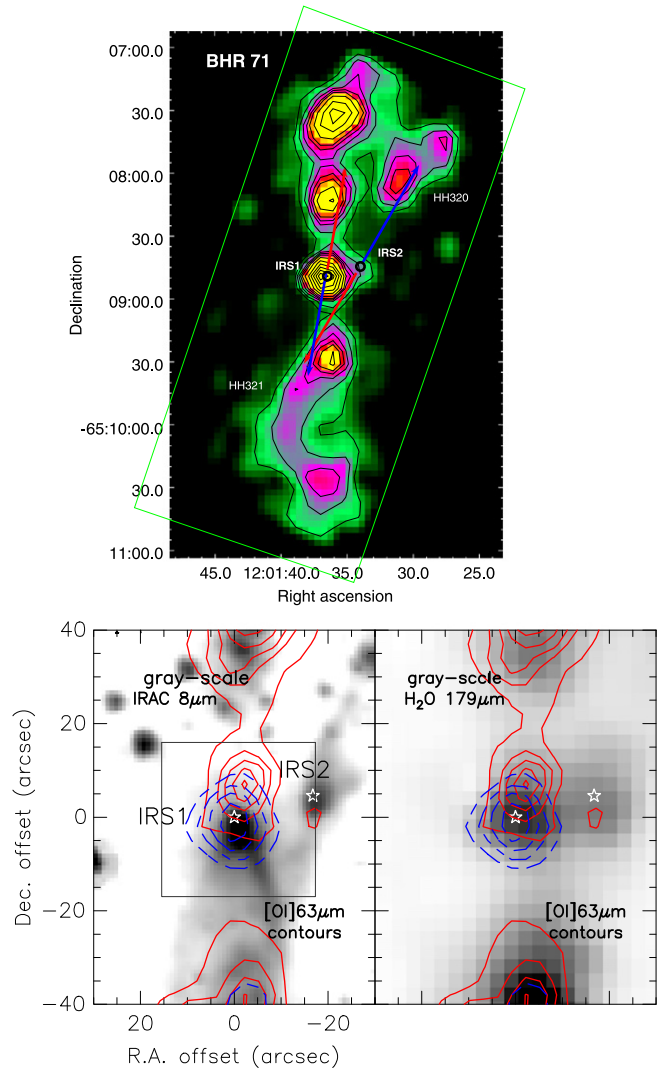
Figure 4. As in Figure 1, but for BHR 71. The arrows in the upper map indicate the directions of the blue- and redshifted lobes of the two outflows from the IRS1 and IRS2 sources. In the bottom figure, redshifted contours run from 1.5×10^{-5} to 7.5×10^{-5} erg s^{-1} cm^{-2} sr^{-1} in steps of 1.5×10^{-5} erg s^{-1} cm^{-2} sr^{-1}, while blueshifted contours run from 1.0×10^{-4} to 4.0×10^{-4} erg s^{-1} cm^{-2} sr^{-1} in steps of 1.0×10^{-4} erg s^{-1} cm^{-2} sr^{-1}. Velocity integration limits are -200 to 0 km s^{-1} and 0 to $+200$ km s^{-1} for the blue- and redshifted emission, respectively.

kinematics of the gas close to the central source, where we expect the emission to be connected with the presence of the atomic jet.

From Figures 1–5, we see that in all sources the [O I] emission is spatially resolved close to the source and elongated in the direction of the outflow axis. The FWHM width in the direction perpendicular to the outflow is instead consistent with the width of the point-spread function at 63 μm, and thus it appears nonresolved transversely. We therefore interpret the observed emission as coming from a collimated jet and/or from a series of shocked knots aligned along the outflow axis.

For each source, a spectrum from a rectangular region encompassing the [O I] jet emission has been extracted. Table 2 summarizes the spatial extent of these regions, together with the parameters measured for the [O I] line emission. The LSR line velocity and width at FWHM have been measured by fitting the spatially integrated [O I] 63 μm profile with a Gaussian function. Owing to the factor $\sim$3 lower spectral resolution at 145 μm, this line is always unresolved, so we have not extracted any velocity information from its profile.

The observed peak velocities in the integrated spectra are not centered at systemic velocity but span between -53 km s^{-1} (in BHR 71) and $+56$ km s^{-1} (in *IRAS*4A), i.e., values comparable with the spectral sampling. Spurious wavelength shifts can also be caused by a misalignment of a point-like emitting source with respect to the spaxel center.[13] Although the observed emission is extended over several spaxels, and thus the wavelength shifts should be minimized, we conservatively assume that actual V_{LSR} of the [O I] 63 μm , averaged in the extracted spectra, is between the observed V_{LSR} and the systemic velocity.

In L1448-C, BHR 71 IRS1, and HH 46 IRS the 63 μm line width is significantly larger than the PACS instrumental profile, indicating that the line is spectrally resolved with an intrinsic

---

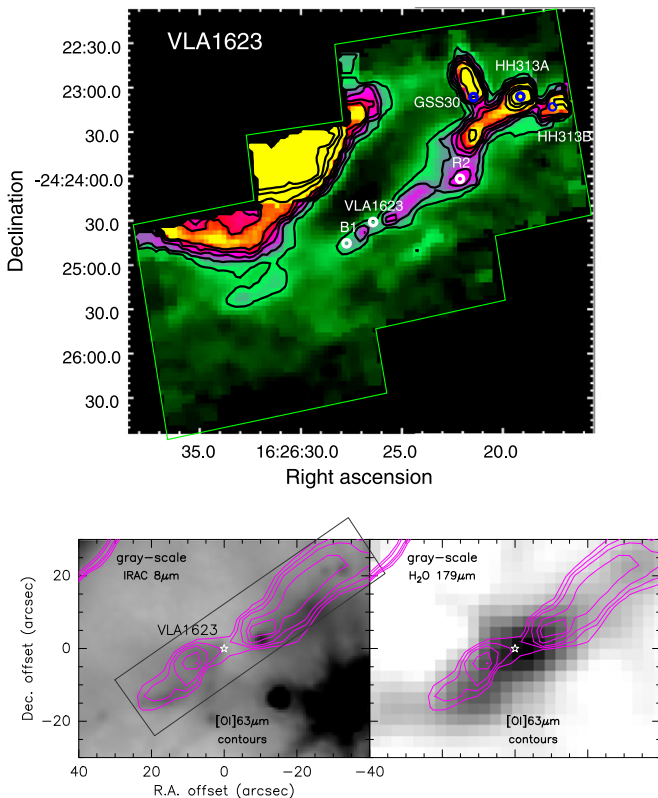[13] See Section 4.7.2 of the PACS observer manual at http://herschel.esac.esa.int/Docs/PACS/html/pacs_om.html.

Figure 5. Same as in Figure 1, but for VLA 1623. Contours refer to the total integrated line intensity and are drawn at the following values: 1.2×10^{-4}, 1.4×10^{-4}, 1.8×10^{-4}, and 2.0×10^{-4} erg s^{-1} cm^{-2} sr^{-1}.

width (measured as $\Delta V_{\rm line} = \sqrt{\Delta V_{\rm obs}^2 - \Delta V_{\rm instr}^2}$) on the order of 110, 90, and 130 km s^{-1} for L1448, BHR 71, and HH 46, respectively. On the other hand, VLA 1623 and IRAS4A have line widths consistent with the instrumental profile and thus are not spectrally resolved.

An enlargement of the region close to the driving source is also presented in Figures 1–5. Here the [O I] emission, shown as contour plots, is superimposed on archival Spitzer IRAC images and, when available, on H$_2$O 179 μm Herschel/PACS maps obtained together with the [O I] observations (Bjerkeli et al. 2012; Nisini et al. 2013; Santangelo et al. 2014; Nisini et al., in preparation). For L1448-C, BHR 71, and HH 46 IRS we have separately integrated the blue- and redshifted line profiles to reveal spatial variations in the gas kinematics. In these sources, the blue and red outflow lobes are spatially separated and are in agreement with the kinematics of the outflow as observed through millimeter tracers (e.g., Bachiller et al. 1990; Bourke et al. 1997; van Kempen et al. 2009).

In L1448-C and VLA 1623, pairs of [O I] emission peaks are symmetrically displaced with respect to the central source, in a similar fashion as the high-velocity millimeter/submillimeter CO/SiO emission associated with molecular jets (e.g., Bachiller et al. 1990; Hirano et al. 2010; André et al. 1990). In IRAS4A, peaks of [O I] 63 μm emission roughly coincide with peaks of the compact CO(6–5) outflow mapped by Yıldız et al. (2012). When compared with H$_2$O, the [O I] emission shows remarkable differences in some of the sources. For instance, in VLA 1623 and IRAS4A, [O I] does not peak toward the central source, at variance with H$_2$O, which peaks on-source in all the objects. This suggests that, at least for these sources, on-source most of the oxygen has been transformed into water by means

of high-temperature reactions or ice evaporation (Elitzur & de Jong 1978). Alternatively, this could indicate that the jet, traced by O I and not by water, is currently not particularly active.

The comparison of [O I] 63 μm with other molecular and atomic species can be seen in detail in L1448, where maps of several tracers at different wavelengths are available. Figure 6 shows an [O I] line intensity cut along the outflow axis, compared with that of H$_2$O 179 μm, H$_2$ 17 μm, and [Fe II] 28 μm lines (from Nisini et al. 2013; Neufeld et al. 2009). Spatial resolution of the 17 and 28 μm Spitzer data is 11$''$ and thus comparable to the [O I] resolution, limited by the PACS spaxel scale, and to the PACS 179 μm diffraction-limited resolution of 12$''$7. Each line intensity is normalized with respect to its maximum. The figure shows that [O I] has a spatial profile very similar to that of [Fe II], with a main peak on-source and secondary peaks approximately around the B2 and R2 shock clumps. H$_2$ does not peak on-source, and the H$_2$O 179 μm emission is slightly less extended than [O I] with no evident peaks on B2/R2. The above evidence suggests that [O I] originates from a shock that is at least partially dissociated, as has been discussed also in Santangelo et al. (2013) and Karska et al. (2013).

In L1448 and HH 46, where the [O I] jet is more extended and the 63 μm line is spectrally resolved, we have extracted the [O I] 63 μm spectra in different positions along the jet, which are displayed in Figure 7. In L1448 the radial velocity changes from blueshifted to redshifted, as one is moving from the northern to the southern position. The same trend is shown in Figure 8, which presents velocity channel maps of the [O I] 63 μm emission. The velocity increases moving away from the driving source, a signature that is more prominent in the redshifted lobe: a similar jet acceleration pattern is also observed in molecular tracers such as SiO (e.g., Guilloteau et al. 1992), which is a further indication that the [O I] emission is physically associated with the millimeter high-velocity jet.

In HH 46, three spectra have been extracted at the on-source and blue/redshifted jet positions (Figure 7). The maximum blue- and redshifted peak velocities are of the order of -180 and $+100$ km s^{-1}, respectively (see also Van Kempen et al. 2010), which are comparable to the velocities of the atomic jet detected in [Fe II] at 1.64 μm (i.e., from -213 to -177 km s^{-1} in the blue lobe and from $+92$ to $+145$ km s^{-1} in the red lobe; Garcia Lopez et al. 2010). [Fe II] emission is also observed at zero velocity but is not as strong as the [O I], likely owing to the extinction. The velocity channel maps are shown in Figure 9: here the acceleration of the jet is not so evident as in L1448, since emission from zero up to high blueshifted velocity is observed on-source, and the peak of the redshifted gas does not shift with velocity.

4. ATOMIC MASS FLUX RATES

The mass flux rate associated with the [O I] jet ($\dot{M}_{\rm jet}$(O I)) is an important quantity to be estimated in order to assess the relevance of the atomic jets in the overall dynamics of the protostellar system.

Given the high quality of our [O I] 63 μm maps and the good, although limited, spatial and spectral resolution, we can adopt two approaches to estimate the mass-loss rates from the observed emission, the first one based on the [O I] 63 μm luminosity and the extent of the emission, and the second one based on shock models. [O I] 63 μm luminosities have been derived from lines fluxes reported in Table 2 assuming the

Table 2
Parameters of [O I] Spectra Extracted in the Jet Regions

| Source | Region | 63 μm | | | | 145 μm |
		$F \pm \Delta F$	V_{LSR}	ΔV	$L/L_\odot$	$F \pm \Delta F$
L1448	$16'' \times 45''$, P.A. = 165°	11.0 ± 0.1	+18	170	1.8×10^{-3}	0.6 ± 0.1
NGC 1333-IRAS4A	$20'' \times 38''$, P.A. = 0	5.3 ± 0.6	+56	130	9.1×10^{-4}	0.5 ± 0.1
HH 46	$32'' \times 59''$, P.A. = 45	32.0 ± 0.6	+32	184	2.0×10^{-2}	2.3 ± 0.1
BHR 71	$33'' \times 33''$, P.A. = 0	26 ± 0.1	−53	160	3.2×10^{-3}	2.0 ± 0.4
VLA 1623	$19'' \times 78''$, P.A. = 125°	46 ± 0.5	+44	125	2.1×10^{-3}	2.2 ± 0.5

Note. The considered rectangular regions are centered on-source. Flux F in units of 10^{-13} erg s^{-1} cm^{-2}. [O I] 63μm luminosity is computed from reported fluxes assuming distances in Table 1. V_{LSR} and ΔV are in km s^{-1}. ΔF is the 1σ statistical error: an additional flux calibration error of ∼20% needs to be considered. ΔV is the observed line FWHM, not deconvolved for the instrumental profile.
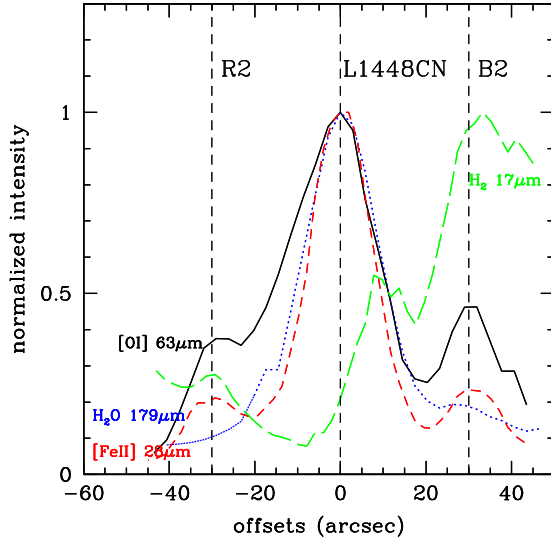

Figure 6. [O I] 63 μm line intensity cut of the L1448-C outflow along its axis (solid line), compared with the intensity of the H$_2$O 179 μm (dotted line; from Nisini et al. 2013), H$_2$ 17 μm (long-dashed line), and [Fe II] 28 μm (dashed line) emissions (from *Spitzer*-IRS observations; Neufeld et al. 2009). The x-axis indicates the offset, in arcseconds, with respect to the L1448-CN source (at coordinates 03:25:38.8, +30:44:09.3). The offsets of the two bright shock knots B2 and R2 are indicated with vertical lines.

distances of Table 1. The computed values are also reported in Table 2. The comparison between the results from the two methods will allow us to evaluate the goodness of the assumptions and approximations embedded in each approach.

4.1. $\dot{M}_{jet}$ (O I) from Line Luminosity

Assuming a steady flow, the mass flux rate can be measured according to the following expression.

$$\dot{M} = \mu m_H \times (n_H \, V) \times V_t/l_t,$$

where μ is the mean particle weight per H nucleus taken equal to 1.4 (Kauffmann et al. 2008) and V_t and l_t are the jet tangential velocity and its length projected onto the plane of the sky, respectively. The latter is taken as the length of the spatial region considered for the [O I] flux extraction, as given in Table 1. The product ($n_H \, V$) of the hydrogen nuclei density and the emitting volume of gas can be related to the [O I] 63 μm observed luminosity, under the assumption of an optically thin

line, as follows:

$$n_H \, V = L([O\,I]63\,\mu m)(h\,\nu A_i f_i X[O])^{-1}.$$

where A_i is the spontaneous radiative rate and f_i the relative level population. The quantity $\epsilon = h\,\nu A_i f_i X[O]$ is the line emissivity per H nucleus (in erg s^{-1}), which depends on the kinetic temperature T_{kin} and on the density of the colliders n_{coll}. $X(O)$ is the atomic oxygen abundance, which we assume here to be equal to the solar value 4.6×10^{-4} (Asplund et al. 2005). We remark that the line luminosity depends on which l_t scale has been used to extract the line flux, so that the quantity $L([O\,I]63\mu m)/l_t$ does not change significantly with the adopted jet length.

To compute the mass flux rate, we therefore need to give constraints on the gas physical conditions and on the tangential velocity of the jet. In principle, we could derive the [O I] jet tangential velocity from the observed radial velocity assuming an outflow inclination angle. However, the limited PACS spectral resolution and the large uncertainty associated with the velocity measurement (see Section 3) prevent us from estimating V_t directly from the PACS spectra. We instead estimate V_t from the proper-motion observations or from radial velocity of the associated high-velocity molecular jet. The adopted values are given in Table 3, and a detailed account on how they have been derived for each source is given in Appendix B. The uncertainty on V_t is expected to vary between 20% and 100%, depending on how well the jet inclination angle and/or proper motion is known.

4.1.1. [O I] 63 μm Physical Conditions and Optical Depth Effects

An estimate of the hydrogen particle density is obtained from the [O I] 63 μm/[O I] 145 μm line ratio, adopting a non-LTE (NLTE) code that considers the first five levels of oxygen. The results are shown in Figure 10, where this ratio is displayed as a function of the density for different values of gas temperatures. The observed line ratios obtained from fluxes measured in the jet regions and reported in Table 2 are here indicated with straight lines. The considered regions are always larger than the 145 μm beam of 11''; hence, we consider negligible flux losses due to diffraction.

We remark that the 63 μm/145 μm ratio does not change significantly, within the errors, from the on-source position to the positions along the outflows. This indicates that we do not appreciate variations of conditions along the jet and also that the 63 μm line on-source does not significantly suffer from line-of-sight extinction from the dusty envelope. The region considered for HH 46 IRS has not been mapped in the 145 μm
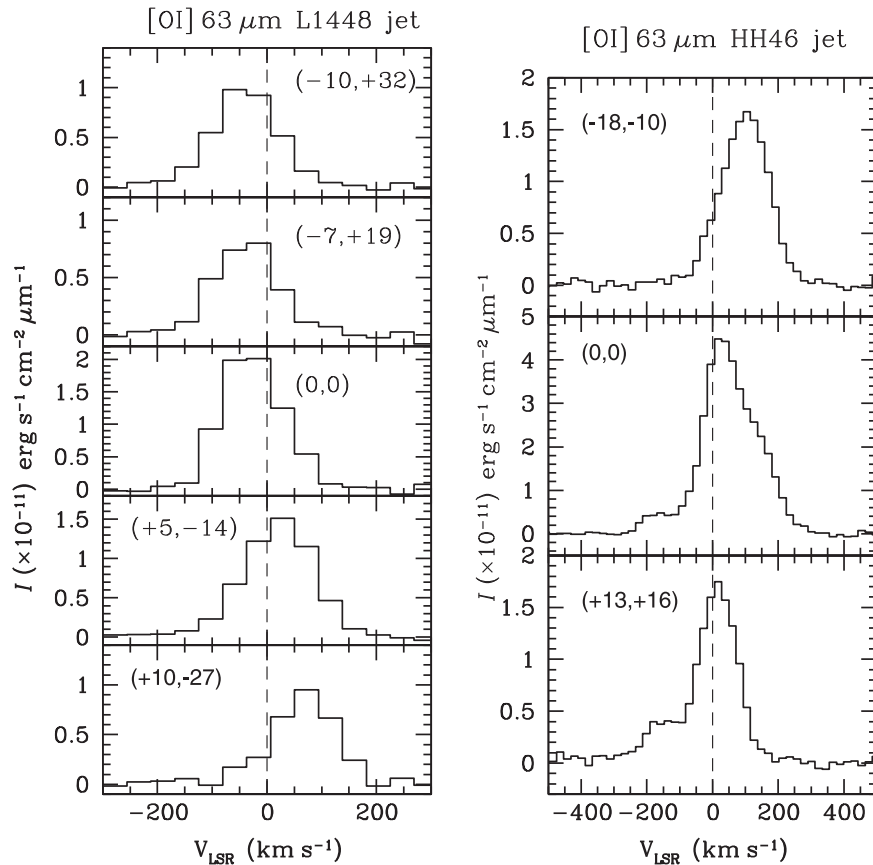
Figure 7. Spectra of the [O I] 63 μm line of 15″ × 15″ rectangular regions centered at the offsets with respect to the central source, indicated in each panel. Left for L1448 and right for HH 46.

line: for this source we therefore consider the 63 μm/145 μm ratio measured in Karska et al. (2013) within a single PACS footprint (47″ × 47″) centered on-source.

Collisions with neutral and molecular hydrogen are considered: since the fraction of H_2 molecules surviving in the [O I] emission region is not known, we consider the two extreme cases of an H gas purely atomic and purely molecular. The line ratios observed in the five sources fall in a region of the plot where the theoretical ratio is rather insensitive to the temperature; however, the uncertainty on the H_2/H ratio translates into an uncertainty of about an order of magnitude in the derived (H + H_2) density, with larger densities obtained for the fully molecular case.

The emissivity of the [O I] 63 μm line changes by at most a factor of three for kinetic temperatures T_k larger than 300 K (see, e.g., Figure 7 of Liseau & Justtanont 2009). The uncertainty on the colliders' density eventually results in a factor between two and five in the line emissivity, for densities less than 10^5 cm^{-3}.

In the above estimate, we have always assumed the [O I] 63 μm as being optically thin. To evaluate whether we can disregard opacity effects in the line emissivity estimates, we have used the Radex radiative transfer code (van der Tak et al. 2007), assuming the large velocity gradient approximation, to calculate for which values of H column density the opacity starts to be significant. The result is shown in Figure 11, which plots, as a function of density, the column density of atomic hydrogen at which τ([O I] 63 μm) is equal to 1. Here a line width of 20 km s^{-1} has been assumed. We see that for the

range of inferred densities, column densities larger than 10^{22} cm^{-2} are required to have an appreciable opacity in the line. Assuming that the [O I] emission originates in a jet with uniform density, the derived N(H) limit would imply, for a density of 10^4 cm^{-3}, a jet diameter larger than 0.3 pc, which is clearly not consistent with observations. Similar conclusions are reached if one assumes the colliders to be fully molecular.

More significant could be the effect of [O I] 63 μm absorption by the cold gas along the line of sight, which would not be observed on the spectra owing to the limited PACS spectral resolution. Such an absorption should not affect the [O I] 145 μm, if we assume that the oxygen in the cold foreground gas is mostly populated in the ground level. Absorption by foreground gas was suggested to explain the very low (i.e., down to ∼1) [O I] 63 μm/[O I] 145 μm line ratios observed with *ISO*-LWS toward young stars (e.g., Liseau et al. 2006). As seen in Figure 10, our [O I] 63 μm/[O I]145 μm ratios are between 12 and 20: predictions from shock models give values between 10 and 35, depending on preshock densities and shock velocities (Hollenbach & McKee 1989). Therefore, if foreground absorption is present, it should affect the observed [O I] 63 μm intensity by at most a factor of two, which would increase our density estimates by a factor of ∼10. Taking this possibility into account, the combination of increased density and intrinsic line intensity would result in a decrease of the final mass flux determination of a factor ∼2–3.

In Table 3, the ranges of the mass flux values derived from line luminosity ($\dot{M}_{jet}^{lum}$(O I)) are reported for each jet, taking into account the above-discussed uncertainties. The uncertainty
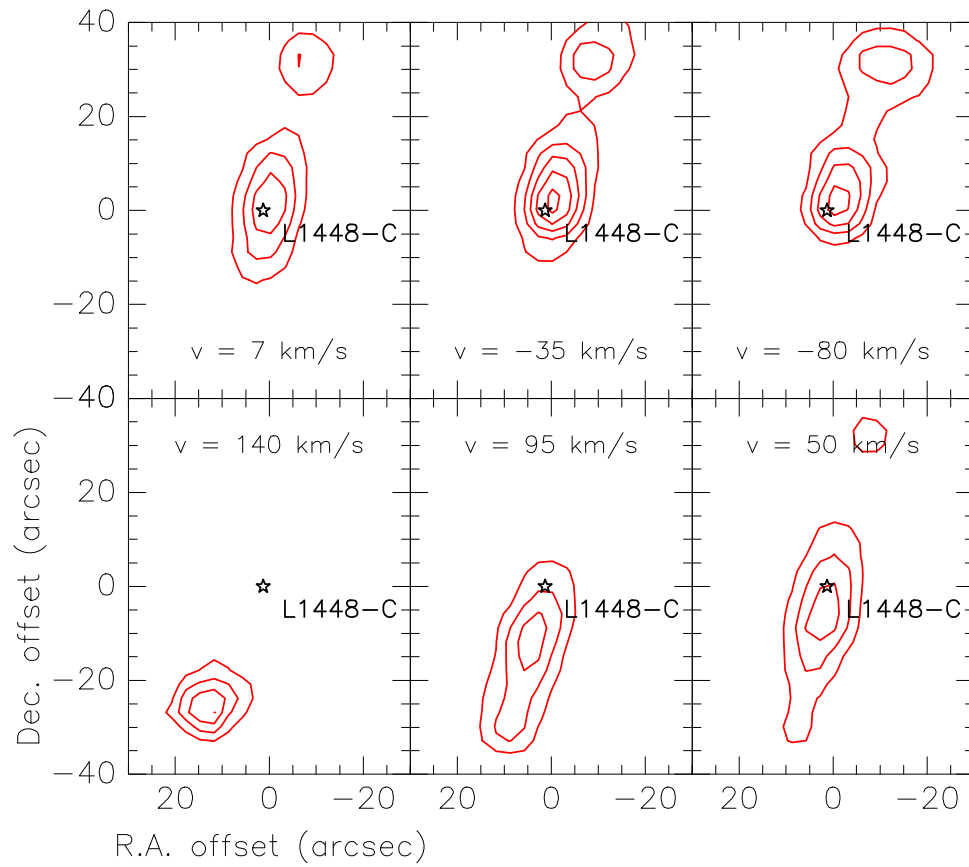
Figure 8. Velocity channel maps of the L1448-C [O I] 63 μm emission. Each map represents a PACS spectral slice centered at the indicated velocity bin and covering half the nominal instrumental spectral resolution, i.e., about 44 km s^{-1}.
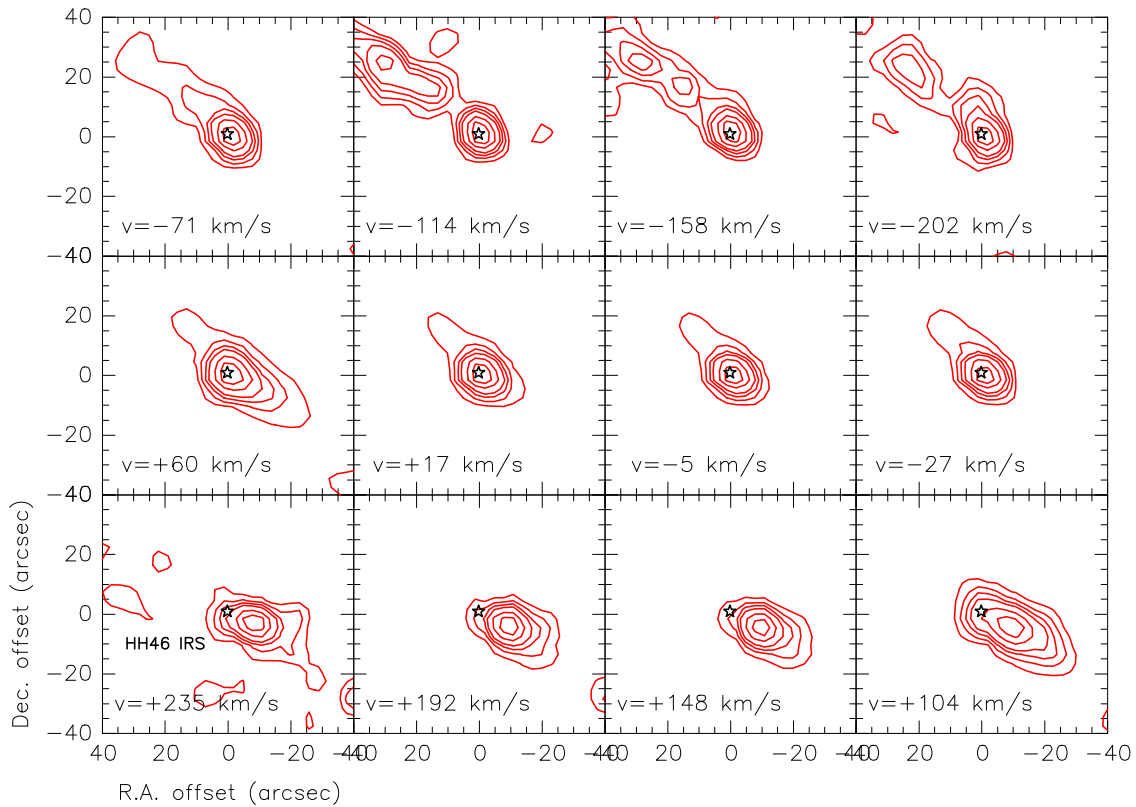

Figure 9. Same as in Figure 8, but for the HH 46 flow.

Table 3
[O I] Mass Flux Rate Estimates and Comparison with $\dot{M}_{jet}$(CO) and $\dot{M}_{acc}$

Source	$n(H+H_2)$	V_t	$\dot{M}_{jet}^{lum}$(O I)[a]	$\dot{M}_{jet}^{shock}$(O I)[a]	$\dot{M}_{jet}$(CO)[b]	Ref.[c]	$\dot{M}_{acc}$ [d]
	$(10^4$ cm$^{-3})$	(km s^{-1})		$(10^{-7}\ M_\odot$ yr$^{-1})$			$(10^{-6}\ M_\odot$ yr$^{-1})$
L1448	1–10	170	2–4	2–4	27–110	1/2/3/4	3.7
IRAS4A	0.1–3	100–140	1.2–11	1–2	1.5–38	4/5/6	3.8
HH 46	0.4–6	300	22–88	20–40	15–28	4/7	12
BHR 71	0.2–3	50–100	2–4	3–6	42–530	4/8	6.2
VLA 1623	2–20	60	1–4	2–4	16–160	9	0.5

[a] $\dot{M}_{jet}^{lim}$(O I) is the mass flux rate measured from the [O I] 63 μm luminosity following the procedure in Section 4.1. $\dot{M}_{jet}^{shock}$(O I) is the mass flux rate derived following Hollenbach (1985).

[b] $\dot{M}_{jet}$(CO) is the mass-loss rate in the original jet/wind needed to drive the CO large-scale outflow assuming momentum conservation, and it has been estimated as $\dot{M}_{jet}$(CO) $\times V_{jet} = F_{CO}$, where F_{CO} is the measured outflow force in $M_\odot$ yr^{-1} km s^{-1}.

[c] References for the outflow parameters are (1) Bachiller et al. (1990), (2) Hirano et al. (2010), (3) Gomez-Ruiz et al. (2013), (4) Yıldız et al. (2014), (5) Knee & Sandell (2000), (6) Blake et al. (1995), (7) van Kempen et al. (2009), (8) Bourke et al. (1997), (9) André et al. (1990).

[d] $\dot{M}_{acc}$ estimated assuming that L_{bol} given in Table 1 is dominated by the accretion luminosity and that $M_* = 0.2\ M_\odot$.
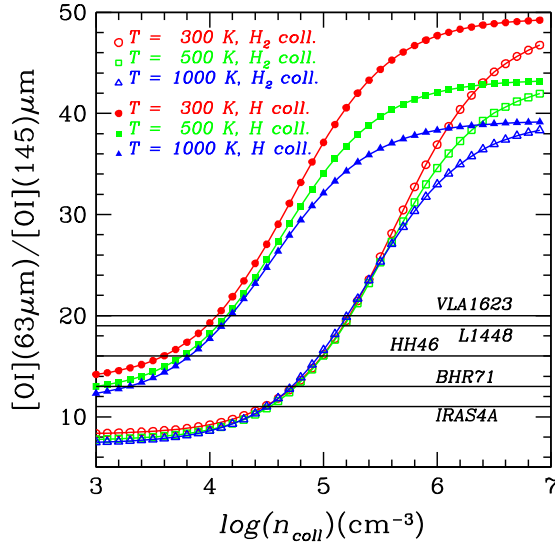

Figure 10. [O I] 63 μm/145 μm theoretical NLTE line intensity ratio plotted as a function of density for three different temperature values. Open and filled symbols indicate the predictions assuming collisions with molecular and neutral hydrogen, respectively. Horizontal lines indicate the values of the ratio observed in the objects of our sample. Observational errors on the ratios are of the order of 20%. Note that not knowing the composition of the colliding particles introduces an uncertainty of about a factor of 10 in the derived densities.

Figure 11. Hydrogen column density vs. volume density of atomic hydrogen, for unit optical depth in the [O I] 63 μm emission line. An oxygen abundance of 4.6×10^{-4} with respect to H is assumed, as well as a line width of 20 km s^{-1}.

on the density dominates the final error of the $\dot{M}_{jet}^{lum}$(O I). Values range between 10^{-7} and 7×10^{-6} $M_\odot$ yr^{-1}, with the largest value found in HH 46.

4.2. $\dot{M}_{jet}$(O I) from Shock Model

Several lines of evidence suggest that the observed [O I] emission has its origin in dissociative shocks occurring within the jet. First of all, [O I] spatially correlates with [Fe II] (see Figure 6), whose emission is associated with dissociative shocks. In fact, C-shocks do not produce a high enough degree of ionization to guarantee efficient electronic collisions of [Fe II] lines (Giannini et al. 2004). In addition, analysis of [O I] lines in several Class 0 shock spots shows that [O I] cannot be accounted for by the same nondissociative shock giving rise to the high-J CO and H$_2$O emission (Santangelo et al. 2013;
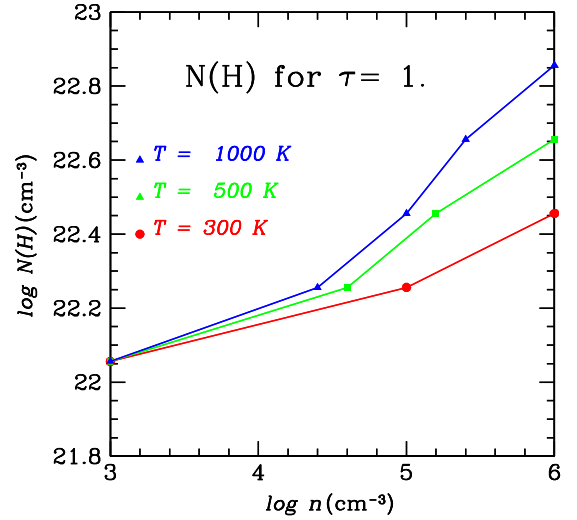
Benedettini et al. 2012). A similar conclusion on the source position has been found by Karska et al. (2014) from the analysis of the PACS data of a sample of Class 0 and Class I sources.

Under the assumption that the [O I] emission is connected with dissociative jet shocks, we can estimate the mass-loss rate adopting models of Hollenbach & McKee (1989), which predict that $\dot{M}$ is directly proportional to the observed [O I] 63 μm luminosity provided that the product of the preshock density (n_o) and shock velocity (V_{shock}) is $n_o \times V_{shock} \lesssim 10^{12}$ cm^{-2} s^{-1} (Hollenbach 1985):

$$\dot{M}_{shock} = 10^{-4}\left(L\left([O\ I]63\mu m\right)/L_\odot\right)M_\odot\ yr^{-1}.$$

The above relationship assumes that L([O I] 63 μm) is all emitted in a single shock caused by the jet/wind launched material impacting on the slow ambient gas, with $V_{shock} \sim V_{jet}$. More realistically, the emission we observe is caused by several unresolved shocks along the jet, having velocities smaller than the total jet velocity (typical J-shock velocities in atomic jets from Class II sources are of the order of 30–40 km s^{-1}, i.e.,
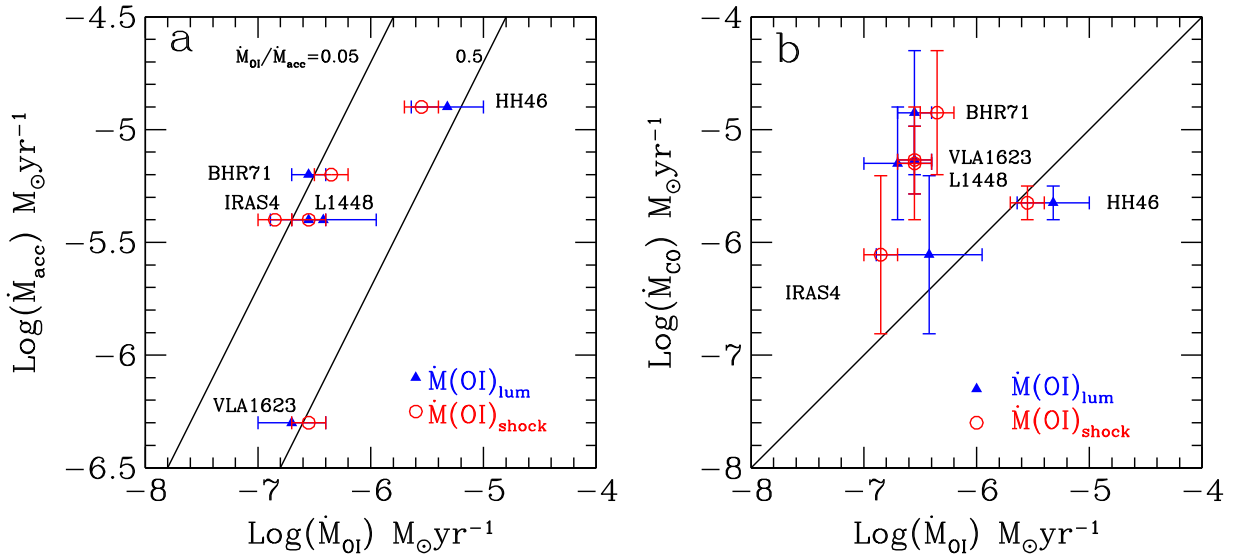
Figure 12. Comparison between (a) the [O I] atomic mass flux determinations and the protostellar mass accretion rate and (b) the wind mass flux needed to sustain the CO outflow (see details in Section 4). Blue triangles and red circles refer to mean values of the determinations obtained from the [O I] 63 μm luminosity and from the Hollenbach (1985) formula that assumes that the 63 μm line originates from the dissociative wind shock, respectively. Error bars denote the range of the determinations.

about 3–6 times smaller than the jet velocities; e.g., Hartigan et al. 1995). Therefore, one should, in principle, correct the above relationship for these effects, by multiplying it by the term $(V_{jet}/V_{shock} \times (1/N_{shock}))$, where N_{shock} is the number of shocks in the jet. Under the reasonable assumption that in the considered jet sections the number of shocks is of the order of a few, the correction term should be of the order of unity and thus will not be further considered.

In Table 3, the values of mass flux rates computed from the Hollenbach (1985) formula $(\dot{M}_{jet}^{shock}(O I))$ are reported and compared with the previous estimates from line luminosity. These two independent methods give results that are in striking agreement with each other, in spite of the different assumptions. This may, however, be not totally fortuitous since both methods are based on the [O I] 63 μm line luminosity. The main difference is that in one case the line theoretical emissivity is computed assuming specific physical conditions, while in the shock case it is assumed that [O I] is the main coolant in the postshock gas for temperatures from $\sim$5000 to $\sim$300 K and that each particle entering the shock radiates in the 63 μm line about $1.5 \times kT$ with $T \sim 5000$ K.

5. DISCUSSION

The PACS observations reveal the presence of atomic collimated emission associated with the outflows of five Class 0 sources. We wish to examine the role of this emission in the global energy budget of the protostellar system. In particular, we can estimate the $\dot{M}_{jet}(O I)/\dot{M}_{acc}$ ratio, with $\dot{M}_{acc}$ the mass accretion rate onto the protostar, to evaluate the efficiency of the atomic jet in removing matter from the accreting system. At the same time, we can also discuss whether this atomic jet possesses enough momentum to sustain the entrained large-scale and powerful CO outflows associated with the considered sources.

Measurements of $\dot{M}_{acc}$ in Class 0 sources are difficult and have a large uncertainty, because the accretion region is obscured from direct view by the optically thick massive envelope and because the already-accumulated stellar mass is

generally unknown. A rough estimate of $\dot{M}_{acc}$ can be obtained by assuming that the source bolometric luminosity is dominated by accretion and that the mass of the central star is 0.2 $M_\odot$. The latter assumption is supported by recent interferometric observations of rotating disks in VLA 1623 and similar Class 0 sources, inferring stellar masses around 0.2 $M_\odot$ (Murillo et al. 2013; Codella et al. 2014). Taking the bolometric luminosities given in Table 1 and further assuming $R_\star \sim 4\,R_\odot$, we derive mass accretion rates ranging from 0.5 to $12 \times 10^{-6}\,M_\odot\,yr^{-1}$. Figure 12(a) shows the derived $\dot{M}_{acc}$ as a function of the $\dot{M}_{jet}(O I)$, where both determinations, from [O I] 63 μm luminosity and the shock model, have been considered (blue triangles and open red circles, respectively). $\dot{M}_{jet}(O I)/\dot{M}_{acc}$ ratios are in the range 0.05–0.5. These values are in line with current MHD jet launching models (e.g., Ferreira et al. 2006), where mass-loss rates are predicted to be $\sim$0.05–0.5 of the mass accretion rate, and they are also consistent with the $\dot{M}_{jet}(O I)/\dot{M}_{acc}$ ratios measured in more evolved Class I and CTTS sources, for which values in the range 0.05–0.4 are typically found (Antoniucci et al. 2008; Ellerbroek et al. 2013).

The role of the [O I] jet on the overall outflow dynamics can also be addressed by comparing the [O I] mass flux with estimates of the outflow thrust (or force, F_{CO}). The latter is usually inferred from millimeter observations of the CO emission. Derivation of F_{CO} is subject to a large uncertainty due to the different methods used to determine outflow mass and the different corrections for observational effects, such as opacity and inclination (see, e.g., Downes & Cabrit 2007; van der Marel et al. 2013). If the outflow is driven by the underlying jet with momentum conservation, then the (total) jet mass-loss rate and outflow thrust should be related by $\dot{M}_{jet}(CO) = F_{CO}/V_{jet}$. V_{jet} is the total jet velocity that can be estimated from the jet radial velocity and inclination angle following the same considerations adopted for the tangential velocity in Appendix B. Literature determinations of $\dot{M}_{jet}(CO)$ are reported in Table 3 for each outflow; the corresponding

range of values in some cases spans up to an order of magnitude.

The resulting $\dot{M}_{\rm jet}({\rm O\,I})$ versus $\dot{M}_{\rm jet}({\rm CO})$ plot is shown in Figure 12(b): we note here that for two of the sources, namely, NGC 1333-*IRAS*4A and HH 46 IRS, the two mass-loss determinations are consistent within the errors, indicating that the [O I] jet may have a role in driving the large-scale outflow. For the other three sources, however, $\dot{M}_{\rm jet}({\rm O\,I})$ is more than an order of magnitude smaller than the value needed to sustain the outflow, even taking into account the large $\dot{M}_{\rm jet}({\rm CO})$ uncertainty. Comparing the results in Figures 12(a) and 12(b), it appears clear that the mass flux derived from CO in L1448, VLA 1623, and BHR 71 is in contradiction with the $\dot{M}_{\rm acc}$ estimated from their bolometric luminosity, since it implies $\dot{M}_{\rm jet}({\rm CO})/\dot{M}_{\rm acc} \geqslant 1$.

Therefore, for these three sources either the $\dot{M}_{\rm jet}({\rm CO})$ is largely overestimated or $\dot{M}_{\rm acc}$ is underestimated, owing, for example, to a central mass lower than assumed. In the latter case, $\dot{M}_{\rm jet}({\rm O\,I})$ in these three sources would be $<0.01\,\dot{M}_{\rm acc}$ and thus insufficient both to account for driving the outflow and to have a role in limiting the accreting material onto the star.

Of the three sources, BHR 71 has more uncertainty in the $\dot{M}_{\rm jet}({\rm CO})$ estimation, because the inclination of the outflow is poorly known and because there is the contamination by the secondary outflow from IRS2. In the case of the VLA 1623 outflow, the larger error in the thrust determination comes from disentangling the outflow gas at low radial velocity from the envelope gas because of the low outflow inclination with respect to the plane of the sky. André et al. (1990), however, estimate that the error due to this effect would not change the outflow mass by a factor of more than two.

Finally, the outflow force in L1448 has been measured by different authors adopting different data and methods. In particular, the value originally measured with single-dish, low-*J* line observations (Bachiller et al. 1990) has been confirmed with the analysis of high-resolution interferometric (Hirano et al. 2010) and high-*J* CO (Gomez-Ruiz et al. 2013; Yıldız et al. 2014) observations. It is therefore unlikely that all those determinations are overestimated by a factor of 10. In order to reconcile the high CO mass ejection rate in L1448 with its low bolometric luminosity, Hirano et al. (2010) assume that the protostellar mass should be in the range 0.03–0.09 $M_\odot$. Time variability in the disk accretion rate could also be at the origin of the found discrepancy.

We note that the CO outflow of L1448 is peculiar with respect to the others, since it presents extreme high velocity (EHV) molecular gas in the form of CO/SiO collimated emission, corresponding to deprojected velocities of the order of about 200 km s^{-1} (Bachiller et al. 1990; Hirano et al. 2010). Interferometric millimeter observations of this emission suggest that it may be directly linked to the original protostellar jet and not to entrained material. This is also supported by the very different chemical composition of the EHV gas compared to the lower-velocity outflow gas, pointing to a different origin of the two components (Tafalla et al. 2010). The above findings suggest that the primary jet responsible for driving the large-scale low-velocity outflow of L1448 is mainly molecular and that the atomic gas contributes only for a smaller part to the total jet momentum. Dionatos et al. (2009) discovered for the first time the atomic jet in L1448 with *Spitzer*, through its [S I] and [Fe II] mid-IR emission. The mass flux derived for this atomic emission, detected through single-pointing IRS

observations, was in the range $(2–20) \times 10^{-7}\,M_\odot$ yr^{-1}, which is consistent with the values derived here from [O I]. An evaluation of the relative contribution of the atomic and molecular jet to the dynamics of the outflow can be done in L1448, since Hirano et al. (2010) computed the CO force separately for the EHV jet and for the outflow low-velocity shell. The $F_{\rm CO}$ of the molecular jet is $\sim 5 \times 10^{-4}\,M_\odot$ km s^{-1} yr^{-1}, implying a mass flux rate of $\sim 4 \times 10^{-6}\,M_\odot$ yr^{-1} for a jet velocity of 180 km s^{-1}, which is an order of magnitude higher than $\dot{M}_{\rm jet}({\rm O\,I})$. $F_{\rm CO}$ of the slow swept-out gas is instead of the order of $1.8 \times 10^{-3}\,M_\odot$ km s^{-1} yr^{-1}, i.e., about a factor of three higher than the force of the jet. Given the involved uncertainties, the EHV jet could indeed be the main agent in driving the slow-speed shells.

No CO jet-like emission has been mapped in VLA 1623 and BHR 71, due to the lack of high-resolution observations; it is, however, remarkable that they both show evidence of EHV gas with deprojected velocities in excess of 70 km s^{-1} (André et al. 1990; Kristensen et al. 2012). This may suggest that also in these two sources the discrepancy between $\dot{M}_{\rm jet}({\rm CO})$ and $\dot{M}_{\rm jet}({\rm O\,I})$ could be due to the fact that the atomic [O I] jet represents only a minor component of the original jet and that the latter is mainly composed of molecular material.

HH 46 is the more evolved of the sampled sources, being classified between the Class 0 and Class I stage (Antoniucci et al. 2008), and has an already well-developed atomic jet observed in high-excitation optical and near-IR forbidden lines. The mass flux rate of the jet has been estimated to be in the range $(0.5–1) \times 10^{-7}\,M_\odot$ yr^{-1} from the near-IR [Fe II] emission (Garcia Lopez et al. 2010). This value is smaller by a factor of at least 20 compared to that inferred from [O I] 63 μm. This reinforces the result of Figure 12, i.e., that in this source the large-scale outflow is mainly sustained from the low-excitation neutral atomic jet traced by the [O I] 63 μm emission.

The above findings are in line with the idea that jets undergo an evolution in their composition. Jets in the youngest sources remain mainly molecular while the atomic component progressively becomes dominant, as the jet gas excitation and ionization increase. Jets from more evolved pre-main-sequence T Tauri stars are in fact bright in UV–optical lines showing larger ionization fractions, $(x_e \sim 0.2$–$0.5)$ and electron temperatures $(T_e \sim (0.5$–$2) \times 10^4$ K) with respect to younger Class I sources (having $x_e \sim 0.05$–0.1 and $T_e \sim 10^4$ K; Nisini 2009). Although PACS observations of a few T Tauri stars indicate that the $\dot{M}_{\rm jet}$ derived from [O I] 63 μm is higher than or comparable to the value derived from optical lines (Podio et al. 2012), these values should be considered as upper limits as [O I] emission in these evolved sources could be contaminated by PDR emission (e.g., Karska et al. 2014). Such an evolution of physical parameters and composition is, for example, predicted in disk wind models where irradiation from X-ray and far-UV photons from accretion hot spots are taken into account (Panoglou et al. 2012).

Although the statistics are small and should be confirmed on larger samples of sources, our results suggest that the contribution of warm atomic gas on the overall jet composition is dominant only in an intermediate phase of jet evolution, after the originally molecular gas is getting progressively dissociated (early Class 0), and before the jet becomes mainly hot and ionized (CTTSs).

6. CONCLUSIONS

We have carried out mapping observations of the [O I] 63 μm and 145 μm lines toward protostellar outflows in the L1448, NGC 1333-*IRAS*4, BHR 71, VLA 1623, and HH 46 star-forming regions using the PACS instrument on *Herschel*. We have used these maps to detect atomic jets at low excitation, which could be the responsible agent for driving the large-scale molecular outflows, and to study their dynamical properties.

The main results obtained from this work are the following.

1. We observe, close to the driving sources, spatially resolved [O I] emission extended along the outflow direction, which we attribute to the presence of a collimated jet. This interpretation is reinforced in three out of the five considered sources (namely, L1448, BHR 71, and HH 46), by the kinematics of the [O I] emission; we were in fact able to separate the red- and blueshifted jet lobes, having maximum velocities up to 200 km s^{-1}.

2. In L1448 and HH 46, having the largest velocity spreads, velocity channel maps have been constructed in order to study their variations as a function of distance from the source. The clearest pattern is shown by the [O I] emission in L1448, where we observe that the velocity increases with distance from the driving source: a similar acceleration has been previously observed in the SiO collimated jet associated with this source, suggesting that the [O I] and molecular gas are kinematically connected and that the latter could represent the colder cocoon of a jet at higher excitation.

3. Complementary observations of the [O I] 145 μm line are used to constrain the gas density ($n(\mathrm{H+H_2})$) of the atomic jet between 10^3 and 10^5 cm^{-3} assuming $T_k \gtrsim 300$ K. We additionally infer that self-absorption of the [O I] 63 μm should not be significant, while absorption by cold gas along the line of sight should affect the observed line flux by at most a factor of two.

4. Mass flux rates for the atomic jet ($\dot{M}_{\mathrm{jet}}(\mathrm{O\,I})$) have been measured from the [O I] 63 μm luminosity, adopting two independent methods. The first one is based on the [O I] 63 μm luminosity and emission extent and needs to assume the gas physical conditions and tangential velocity, while the second one is based on the assumption that the emission comes from the dissociative shock occurring when the primary jet/wind interacts with the ambient medium. The two determinations are consistent with each other and provide values in the range $(1–4) \times 10^{-7}\,M_\odot$ yr^{-1} for L1448, *IRAS*4A, BHR 71, and VLA123 and an order of magnitude higher value for HH 46.

5. The derived mass flux rates are compared with mass accretion rates ($\dot{M}_{\mathrm{acc}}$) to the central protostar and the $\dot{M}_{\mathrm{jet}}$ (CO) estimated from the large-scale cold CO maps, assuming momentum conservation in the interaction between the jet and the ambient medium. We find $\dot{M}_{\mathrm{jet}}$ (O I)/$\dot{M}_{\mathrm{acc}}$ ratios in the range 0.05–0.5, similar to values found in more evolved Class I/II sources.

The $\dot{M}_{\mathrm{jet}}(\mathrm{O\,I})$ is comparable to $\dot{M}_{\mathrm{jet}}(\mathrm{CO})$ in only two sources, namely, HH 46 and *IRAS*4 A, while it is more than an order of magnitude smaller than $\dot{M}_{\mathrm{jet}}(\mathrm{CO})$ in the remaining three, L1448, VLA 1623, and BHR 71. Since these three sources with smaller $\dot{M}_{\mathrm{jet}}(\mathrm{O\,I})$ are associated with the molecular gas at extreme velocities, we speculate that most of the mass flux is carried out by the molecular jet and that the contribution of the atomic jet to the acceleration of the large-scale outflow is less significant.

The above findings suggest an evolution in the properties of jets during the protostellar and pre-main-sequence lifetime. In this scenario, the contribution of warm atomic gas, traced by the [O I] 63 μm line, to the overall jet composition is dominant only in an intermediate phase of jet evolution, after the originally molecular jet gets progressively dissociated (early Class 0), and before it becomes mainly hot and ionized (Class II). [O I] 63 μm mapping of jets from more Class 0 and Class I sources would be needed to increase statistics on the role of the warm atomic gas in the dynamics of protostellar jets. In this respect, observations with the SOFIA-GREAT instrument will provide high enough spectral resolution to obtain velocity-resolved [O I] maps in a larger sample of sources, allowing one to study the dynamics of the [O I] protostellar jets in much more detail.

APPENDIX A
OUTFLOW DESCRIPTIONS AND [O I] GENERAL MORPHOLOGY

L1448: located in the Perseus molecular cloud ($D = 232$ pc; Hirota et al. 2011), the low-luminosity Class 0 source L1448-C (or L1448-mm) drives a powerful and extended molecular outflow (Bachiller et al. 1990) that interacts in the northen region, with two other compact flows originating from the small three-star cluster L1448-N (Looney et al. 2000). L1448-C itself is in fact a binary (CN and CS; Jørgensen et al. 2006) with the CN source responsible for the excitation of this extended outflow. Close to the driving source, interferometric CO and SiO observations have resolved the outflow into two kinematically distinct components; a very collimated and high-velocity component seen in both CO and SiO, and low-velocity cavity walls only seen in CO (Hirano et al. 2010). Warm molecular gas, with temperature in excess of ~300 K, has been probed by different near- and far-IR observations of H_2, CO, and H_2O all along the outflow (Nisini et al. 2000, 2013; Davis & Smith 1996; Neufeld et al. 2009; Giannini et al. 2011; Santangelo et al. 2013). *Spitzer* observations have provided evidence for the presence of an atomic jet at low excitation, emitting in [S I], [Fe II], and [Si II] lines (Dionatos et al. 2009). The [O I] 63 μm map (Figure 1) shows bright emission peaks toward the sources of the field. In particular, elongated jet-like emission is detected toward L1448-CN/S, while the strongest peak is located at the L1448-NA source. Additional peaks are observed along the outflow in correspondence with known shock spots B2/R2, R3, and R4.

NGC 1333-IRAS4: NGC 1333-*IRAS*4 consists of four very embedded objects located in the L1450 dark cloud within the Perseus molecular cloud ($D = 235$ pc; Hirota et al. 2008). *IRAS*4A and B are separated by about 30″, and each of them is a binary (A and A', separated by 2″, and B and B', separated by 11″; Lay et al. 1995; Looney et al. 2000). Outflows have been detected in both the A and B sources, but with a very different morphology. The 4A outflow extends more than 4′, has been detected in both CO and SiO, and shows a remarkable directional variability, with the position angle quickly changing

from 0 to about 45° close to the source, and again showing a sharp bend in the middle of the northeastern lobe (Choi et al. 2006). At variance, the *IRAS*4B flow is very compact, extending only for about 20″ from source (Jørgensen et al. 2007; Plunkett et al. 2013). *Herschel* detected strong warm molecular emission from CO and H_2O associated with the outflows of both *IRAS*4A and 4B (Herczeg et al. 2012; Karska et al. 2013; Santangelo et al. 2014).

The PACS map presented in Figure 3 covers the outflows for both *IRAS*4A and 4B. The outflow from *IRAS*4B is very compact, and the [O I] 63 μm emission is offset with respect to the central source, as discussed in Herczeg et al. (2012). Emission is detected along the extended *IRAS*4A outflow with a strong peak on the shocked R2 position, where also H_2O and high-J CO have been detected by *Herschel* (Santangelo et al. 2014).

HH 46: HH 46 IRS is located in an isolated Bok globule close to the Gum nebula (at a distance of 450 pc). It is a highly accreting object (Antoniucci et al. 2008) driving a well-known and spectacular outflow first discovered at visible and IR wavelengths (Eislöffel and Mundt 1994; Heathcote et al. 1996; Hartigan et al. 2005). Optically, the brightest part of the flow is the blueshifted northeastern region, where strong HH objects have been detected with the *Hubble Space Telescope*. The HH 46 IRS redshifted counterjet, moving at radial velocities up to 150 km s^{-1}, has been detected in the infrared from both ground-based and *Spitzer* observations (Velusamy et al. 2007; Garcia Lopez et al. 2010). HH 46 IRS also drives an extended molecular outflow (Chernin & Masson 1991; van Kempen et al. 2009) that has been recently studied at high resolution with ALMA CO(1–0) observations (Arce et al. 2013). The morphology and kinematics of the molecular gas support the presence of a wide-angle wind producing an extended cavity, plus a collimated episodic flow. Far-IR line emission from H_2O, CO, [O I], and OH has been observed both on-source and on the outflow by *Herschel* (Van Kempen et al. 2010).

The [O I] 63 μm map presented here (Figure 5) covers the full extent of the outflow up to the two bright terminal bow shocks HH 47A and HH 47C (e.g., Eislöffel and Mundt 1994). The emission is centrally peaked and extends along the outflow with different emission knots. The two emission peaks at the extreme of the map are located just ustream of HH 47A and HH 47C. This spatial offset between the [O I] 63 μm emission and the HH objects' location is probably just due to a poor sampling at the map edges.

BHR 71: BHR 71 is a close-by isolated Bok globule ($D \sim$ 200 pc), hosting an extended bipolar outflow originating from a binary protostellar system (IRS1 and IRS2; Bourke et al. 1997; Bourke 2001). Further investigations have shown that both sources are driving an outflow: IRS1 is responsible for the extended flow in the north-south direction, while IRS2, the lower-luminosity source, drives a more compact flow having a P.A. of ∼−30° (Parise 2006; Yıldız et al. 2015). The direction of the two outflows is indicated with arrows in Figure 2. Weak optical HH objects (HH 320 and HH 321) have also been detected along the flows (Corporon & Reipurth 1997). The region mapped by our PACS observations covers the central 4′ part of the outflow, which has a length of more than 8′ (∼0.4 pc). The same region investigated here has been mapped with *Spitzer*-IRS, showing bright emission from H_2 mid-IR rotational lines (Neufeld et al. 2009; Giannini et al. 2011). From Figure 2 we see that the [O I] 63 μm has a strong peak

toward the BHR 71-IRS1 source while a much fainter emission is associated with the IRS2 source. Emission peaks are also detected on the cavity walls of the IRS1 and IRS2 outflows, also associated with the HH 320 and HH 321 objects.

VLA 1623: The collimated outflow first discovered by André et al. (1990) in the ρ Oph core A ($D = 120$ pc; Lombardi et al. 2008) is driven by the first-identified Class 0 source object VLA 16234–2417. The source itself was recently discovered to be composed of three different protostellar condensations, two of them, VLA 1623 A and B, separated by only 1″2 (Looney et al. 2000; Maury et al. 2012) and a third faint millimeter source (VLA 1623W) at about 10″ (Murillo et al. 2013). Along the VLA 1623 outflow, several near-IR H_2 knots have been detected (Dent et al. 1995), as well as optical HH objects (HH 313), located close to the reflection nebula of the YSOs GSS 30 (Wilking et al. 1997). A bright nebula, illuminated by the B3 star S1, is located north of VLA 1623 and dominates the mid-IR emission of the region with PAH features (Liseau & Justtanont 2009). A bright PDR is also associated with this nebula and emits strongly in [O I] and [C II] far-IR fine-structure lines (Liseau et al. 1999).

The [O I] 63 μm map (Figure 4) covers the VLA 1623 outflow and part of the PDR, the latter dominating the [O I] emission in the northeast direction. Collimated [O I] 63 μm emission is observed close to the source. Emission is also detected all along the outflow, but the strongest peaks are observed in the weastern lobe, where the HH 313A and 313B objects and the GSS 30 source are located.

APPENDIX B
TANGENTIAL VELOCITY

In this appendix we briefly summarize the derivation of the jet tangential velocity (V_t) adopted for the mass flux determination for each source. These values are reported in Table 3. *L1448:* the maximum radial velocity of the SiO high-velocity jet is 65 km s^{-1} (Guilloteau et al. 1992), and the jet inclination angle has been estimated as 21° (Girart & Acord 2001) with respect to the plane of the sky. This implies a tangential velocity of 170 km s^{-1}. Given the similarity of the [O I] morphology and kinematics with the molecular jet, we assume the same velocity for the [O I] jet.

*IRAS*4: Choi et al. (2006) measured an outflow proper motion of about 100 km s^{-1} from H_2 multiepoch emission. This could be a lower limit to the [O I] jet velocity, since proper motion has been measured on shock knots far from the central source and thus not directly associated with the jet. However, CO observations on source show that the maximum CO radial velocity is of the order of 25 km s^{-1}; even assuming an inclination angle of only 10°, this implies a maximum tangential velocity of 140 km s^{-1}. *HH 46:* Eislöffel and Mundt (1994) measure a proper motion of the HH 46 atomic jet of 200 $\pm$ 100 km s^{-1} and a jet inclination angle of about 30°. Garcia Lopez et al. (2010) measure an [Fe II] 1.64 μm radial velocity in the inner jet of about 200 km s^{-1}. This implies a V_t of 300 km s^{-1}, assuming $\theta = 30°$. *BHR 71:* the inclination angle of this outflow is quite uncertain and has been estimated in the range 25°–65°. Our [O I] PACS map shows that the blue- and redshifted lobes of the atomic jet are quite well separated, favoring an inclination angle of no more than 45°. The maximum radial velocity of the CO high-velocity gas is about 50 km s^{-1}; therefore, we estimate a tangential velocity in the range 50–110 km s^{-1}. *VLA 1623:* Davis et al. (1999) estimate

an inclination angle of $15°$ for this outflow. The CO outflow (André et al. 1990) presents wings up to a maximum of $15 \, km \, s^{-1}$ in the red lobe, which, assuming the inclination of $15°$, corresponds to a maximum tangential velocity of $56 \, km \, s^{-1}$. This is consistent with the proper-motion measurements by Caratti o Garatti et al. (2006) from H_2 observations, which found a tangential velocity in the redshifted jet of $74 \pm 15 \, km \, s^{-1}$.

REFERENCES

Andre, P., Martin-Pintado, J., Despois, D., & Montmerle, T. 1990, A&A, 236, 180

Antoniucci, S., Nisini, B., Giannini, T., & Lorenzetti, D. 2008, A&A, 479, 503

Arce, H. G., Mardones, D., Corder, S. A., et al. 2013, ApJ, 774, 39

Asplund, M., Grevesse, N., & Sauval, A. J. 2005, in ASP Conf. Ser. 336 Cosmic Abundances as Records of Stellar Evolution and Nucleosynthesis, ed. G. Thomas, III Barnes, & N. Bash Frank (San Francisco, CA: ASP), 25

Bachiller, R., Martin-Pintado, J., Tafalla, M., Cernicharo, J., & Lazareff, B. 1990, A&A, 231, 174

Baldovin-Saavedra, C., Audard, M., Güdel, M., et al. 2011, A&A, 528, A22

Benedettini, M., Busquet, G., Lefloch, B., et al. 2012, A&A, 539, L3

Bjerkeli, P., Liseau, R., Larsson, B., et al. 2012, A&A, 546, A29

Blake, G. A., Sandell, G., van Dishoeck, E. F., et al. 1995, ApJ, 441, 689

Bourke, T. L. 2001, ApJL, 554, L91

Bourke, T. L., Garay, G., Lehtinen, K. K., et al. 1997, ApJ, 476, 781

Caratti o Garatti, A., Giannini, T., Nisini, B., & Lorenzetti, D. 2006, A&A, 449, 1077

Ceccarelli, C., Haas, M. R., Hollenbach, D. J., & Rudolph, A. L. 1997, ApJ, 476, 771

Chernin, L. M., & Masson, C. R. 1991, ApJL, 382, L93

Choi, M., Hodapp, K. W., Hayashi, M., et al. 2006, ApJ, 646, 1050

Codella, C., Cabrit, S., Gueth, F., et al. 2007, A&A, 462, L53

Codella, C., Cabrit, S., Gueth, F., et al. 2014, A&A, 568, 5

Corporon, P., & Reipurth, B. 1997, IAU Symp., Low Mass Star Formation-from Inflow to Outflow, 182, ed. F. Malbet, & A. Castets (Paris: IAU), 85

Davis, C. J., Cervantes, B., Nisini, B., et al. 2011, A&A, 528, A3

Davis, C. J., Smith, M. D., Eislöffel, J., & Davies, J. K. 1999, MNRAS, 308, 539

Davis, C. J., & Smith, M. D. J. 1996, A&A, 309, 929

Dent, W. R. F., Matthews, H. E., & Walther, D. M. 1995, MNRAS, 277, 193

Dionatos, O., Nisini, B., Garcia Lopez, R., et al. 2009, ApJ, 692, 1

Downes, T. P., & Cabrit, S. 2007, A&A, 471, 873

Eislöffel, J., & Mundt, R. 1994, A&A, 284, 530

Elitzur, M., & de Jong, T. 1978, A&A, 67, 323

Ellerbroek, L. E., Podio, L., Kaper, L., et al. 2013, A&A, 551, A5

Ferreira, J., Dougados, C., & Cabrit, S. 2006, A&A, 453, 785

Frank, A., Ray, T. P., Cabrit, S., et al. 2014, in Protostars and Planets VI (Tucson, AZ: Univ. Arizona Press), 451

Garcia Lopez, R., Nisini, B., Eislöffel, J., et al. 2010, A&A, 511, A5

Garcia Lopez, R., Nisini, B., Giannini, T., et al. 2008, A&A, 487, 1019

Giannini, T., McCoey, C., Carotti O Garatti, A., et al. 2004, A&A, 419, 999

Giannini, T., Nisini, B., & Lorenzetti, D. 2001, ApJ, 555, 40

Giannini, T., Nisini, B., Neufeld, D., et al. 2011, ApJ, 738, 80

Girart, J. M., & Acord, J. M. P. 2001, ApJL, 552, L63

Gomez-Ruiz, A. I., Wyrowski, F., Gusdorf, A., et al. 2013, A&A, 555, A8

Green, J. D., Evans, N. J., II, Jørgensen, J. K., et al. 2013, ApJ, 770, 123

Gueth, F., & Guilloteau, S. 1999, A&A, 343, 571

Guilloteau, S., Bachiller, R., Fuente, A., & Lucas, R. 1992, A&A, 265, L49

Hartigan, P., Heathcote, S., Morse, J. A., Reipurth, B., & Bally, J. 2005, AJ, 130, 2197

Hartigan, P., & Morse, J. 2007, ApJ, 660, 426

Hartigan, P., Morse, J. A., & Raymond, J. 1995, ApJ, 444, 943

Heathcote, S., Morse, J. A., Hartigan, P., et al. 1996, AJ, 112, 1141

Herczeg, G. J., Karska, A., Bruderer, S., et al. 2012, A&A, 540, A84

Hirano, N., Ho, P. P. T., Liu, S.-Y., et al. 2010, ApJ, 717, 58

Hirota, T., Bushimata, T., Choi, Y. K., et al. 2008, PASJ, 60, 37

Hirota, T., Honma, M., Imai, H., et al. 2011, PASJ, 63, 1

Hollenbach, D. 1985, Icar, 61, 36

Hollenbach, D., & McKee, C. F. 1989, ApJ, 342, 306

Jørgensen, J. K., Bourke, T. L., Myers, P. C., et al. 2007, ApJ, 659, 479

Jørgensen, J. K., Harvey, P. M., Evans, N. J., II, et al. 2006, ApJ, 645, 1246

Karska, A., Herczeg, G. J., van Dishoeck, E. F., et al. 2013, A&A, 552, A141

Karska, A., Kristensen, L. E., van Dishoeck, E. F., et al. 2014, A&A, 572, 9

Kauffman, J., Bertoldi, F., Bourke, T. L., Evans, N. J. II, & Lee, C. W. 2008, A&A, 487, 993

Knee, L. B. G., & Sandell, G. 2000, A&A, 361, 671

Kristensen, L. E., van Dishoeck, E. F., Bergin, E. A., et al. 2012, A&A, 542, A8

Lahuis, F., van Dishoeck, E. F., Jørgensen, J. K., Blake, G. A., & Evans, N. J. 2010, A&A, 519, A3

Lay, O. P., Carlstrom, J. E., & Hills, R. E. 1995, ApJL, 452, L73

Liseau, R., & Justtanont, K. 2009, A&A, 499, 799

Liseau, R., Justtanont, K., & Tielens, A. G. G. M. 2006, A&A, 446, 561

Liseau, R., White, G. J., Larsson, B., et al. 1999, A&A, 344, 342

Lombardi, M., Lada, C. J., & Alves, J. 2008, A&A, 480, 785

Looney, L. W., Mundy, L. G., & Welch, W. J. 2000, ApJ, 529, 477

Maury, A., Ohashi, N., & André, P. 2012, A&A, 539, A130

Murillo, N. M., Lai, S.-P., Bruderer, S., Harsono, D., & van Dishoeck, E. F. 2013, A&A, 560, A103

Neufeld, D. A., Nisini, B., Giannini, T., et al. 2009, ApJ, 706, 170

Nisini, B. 2009, in Protostellar Jets in Context (Berlin: Springer), 215

Nisini, B., Benedettini, M., Giannini, T., et al. 2000, A&A, 360, 297

Nisini, B., Giannini, T., & Lorenzetti, D. 2002, ApJ, 574, 246

Nisini, B., Santangelo, G., Antoniucci, S., et al. 2013, A&A, 549, A16

Panoglou, D., Cabrit, S., Pineau Des Forêts, G., et al. 2012, A&A, 538, A2

Parise, B., Belloche, A., Leurini, S., et al. 2006, A&A, 454, L79

Pilbratt, G. L., Riedinger, J. R., Passvogel, T., et al. 2010, A&A, 518, L1

Plunkett, A. L., Arce, H. G., Corder, S. A., et al. 2013, ApJ, 774, 22

Podio, L., Kamp, I., Flower, D., et al. 2012, A&A, 545, A44

Poglitsch, A., Waelkens, C., Geis, N., et al. 2010, A&A, 518, L2

Santangelo, G., Nisini, B., Antoniucci, S., et al. 2013, A&A, 557, A22

Santangelo, G., Nisini, B., Codella, C., et al. 2014, arXiv:1406.6302

Tafalla, M., Santiago, J., Johnstone, D., & Bachiller, R. 2004, A&A, 423, L21

Tafalla, M., Santiago-García, J., Hacar, A., & Bachiller, R. 2010, A&A, 522, A91

van der Marel, N., Kristensen, L. E., Visser, R., et al. 2013, A&A, 556, A76

van der Tak, F. F. S., Black, J. H., Schöier, F. L., Jansen, D. J., & van Dishoeck, E. F. 2007, A&A, 468, 627

van Dishoeck, E. F., Kristensen, L. E., Benz, A. O., et al. 2011, PASP, 123, 138

van Kempen, T. A., Kristensen, L. E., Herczeg, G. J., et al. 2010, A&A, 518, L121

van Kempen, T. A., van Dishoeck, E. F., Güsten, R., et al. 2009, A&A, 501, 633

Velusamy, T., Langer, W. D., & Marsh, K. A. 2007, ApJL, 668, L159

Wilking, B. A., Schwartz, R. D., Fanetti, T. M., & Friel, E. D. 1997, PASP, 109, 549

Yıldız, U. A., Kristensen, L. E., van Dishoeck, E. F., et al. 2012, A&A, 542, 86

Yıldız, U. A., Kristensen, L. E., van Dishoeck, E. F., et al. 2015, A&A, in press